Modeling, Stability, and Design of the Single-Phase SOGI-Based Phase-Locked Loop Considering the Frequency Feedback Loop Effect

Jinming Xu, *Member, IEEE*, Hao Qian, Qiang Qian, *Member, IEEE*, and Shaojun Xie, *Member, IEEE*

***Abstract*—For single-phase grid-connected inverters, the second-order generalized integrator-based phase-locked loop (SOGI-PLL) is widely used for good harmonics attenuation and frequency adaptability. However, existing studies usually neglect the frequency feedback loop in the modeling and design process, and thus, the potential instability caused by the frequency feedback loop is not well explained. Besides, the improper design of SOGI-PLL can lead to the inverter instability both under ideal and weak grid conditions. Therefore, by fully considering the coupling of the frequency feedback loop, this article establishes an accurate model for SOGI-PLL. Furthermore, effects of different PLL parameters on behaviors of both the SOGI-PLL itself and the inverter are studied, based on which a graphical method for PLL parameters design is proposed. As proved, the frequency feedback loop can deteriorate the stability and performance of both SOGI-PLL itself and inverter system, especially if rapid transient is expected. The modeling method is also extended to the low-pass filter-SOGI-PLL and the improved parameters design is discussed. Experimental results verify the correctness of the proposed PLL model and the abovementioned analysis results. The proposed model is helpful to deeply reveal the instability mechanism and provides a reference for the PLL design under nonideal grid conditions.**

***Index Terms*—Grid-connected inverter, phase-locked loop, second-order generalized integrator, stability, weak grid.**

I. Introduction

TO REALIZE the synchronization between grid-connected inverter (GCI) and the utility grid, the phase-locked loop (PLL) is employed to obtain the phase and frequency of grid voltage at the point of common coupling (PCC) accurately and quickly [1], [2]. In single-phase systems, orthogonal-signal-generator-based PLLs (OSG-PLL) are usually used to achieve the synchronization [3], [4]. Methods for constructing the OSG include: 1/4 period delay [5], first-order differential [6], double Park transform [7], Hilbert transformation [8], and second-order generalized integrator (SOGI) [9]. Among them, the SOGI-PLL has been widely discussed and used because of its simplicity, good filtering ability, and frequency adaptability.

Although the SOGI-PLL has excellent performance under ideal grid conditions, it still faces two problems: 1) instability at a large PLL bandwidth even though under a strong grid; 2) instability of GCI with SOGI-PLL in the weak grid even if the PLL bandwidth is low. As more and more power electronics devices are integrated into the grid, grid situations tend to be more complex (e.g., voltage fluctuation, phase/frequency jump, and variation of grid impedance). Hence, the synchronization unit is required to be fast, accurate, and robust to accomplish the task of phase locking. In other words, PLL should have suitable bandwidth and be able to maintain the system stability under large grid impedance. Such urgent need presents a significant challenge for the SOGI-PLL.

The study in [10] showed that the SOGI-PLL might cause the instability under high PLL bandwidth or large grid impedance, and pointed out that the frequency feedback branch may lead to nonlinear coupling and instability, but the in-depth study on the instability mechanism was missing. In order to avoid the system instability aroused by SOGI-PLL, the frequency-fixed one (i.e., FFSOGI-PLL) is adopted in the case of small or negligible grid frequency fluctuation [11], where the SOGI central frequency keeps at the nominal value, i.e., 50 or 60 Hz. This modification, however, sacrifices the frequency adaptability for the stability. Then, considering large fluctuations of grid frequency, scholars try to abandon the frequency feedback loop (FFL) of PLL itself and propose three types of improvement ways, including: 1) parallel frequency detector method [12], [13], [14]; 2) error calculation based compensation [15], [16]; and 3) modifying the PLL structure [17]. However, these methods tend to increase the control complexity and ignore the PLL dynamics, resulting in tracking errors in the case of frequent frequency fluctuations.

In fact, obtaining accurate PLL model is the key to reveal the instability mechanism, realize the proper design of parameters, and put forward an effective optimization method. However, in the past, scholars mainly considered the characteristics of the phase feedback loop for PLL modeling, and finally obtained a second-order system model reflecting the relation between the phase angle of the input signal and the estimated phase angle of PLL [18]. The second-order system model does not

Manuscript received 22 March 2022; revised 15 June 2022; accepted 12 August 2022. Date of publication 24 August 2022; date of current version 10 October 2022. This work was supported in part by the National Natural Science Foundation of China under Grants 52277184 and 51877104 and in part by the National Key Laboratory of Science and Technology on Helicopter Transmission under Grant HTL-A-22K02. Recommended for publication by Associate Editor G.-S. Seo. *(Corresponding author: Jinming Xu.)*

Jinming Xu, Hao Qian, and Shaojun Xie are with the College of Automation Engineering, Nanjing University of Aeronautics and Astronautics, Nanjing 211100, China (e-mail: xjinming01@163.com; 031520115diyumao@nuaa.edu.cn; eeac@nuaa.edu.cn).

Qiang Qian is with the College of Energy and Electrical Engineering, Hohai University, Nanjing 211100, China (e-mail: qianqiang@hhu.edu.cn).

Color versions of one or more figures in this article are available at https://doi.org/10.1109/TPEL.2022.3201252.

Digital Object Identifier 10.1109/TPEL.2022.3201252

consider the dynamic of OSG, so that the PI parameters of PLL can only be designed from the perspective of damping ratio and bandwidth. Therefore, Golestan et al. [19] included the SOGI into the model and presented a design method considering three aspects (transient performance, stability, harmonic attenuation). However, the abovementioned models are obtained by linearization at the steady-state operating point. For this reason, the study in [20] ignores the influence of FFL and deduces the small-signal transfer function from PLL input voltage to the grid current reference (reconstructed from the PLL estimated phase angle) by using the method of perturbation linearization. Since the error caused by the coupling between different frequency components were not considered in [20], the SOGI-PLL model was obtained by harmonic linearization in [21] and [22] from the perspective of linear time-periodic (LTP) system. But, the effect of frequency feedback branch is still not considered. In [23], the effect of different paths of frequency feedback is studied by solving time-domain state-space equations with the help of MATLAB/Simulink. It indicates the stability boundary under different parameters, but a deep and physical insight is missing for the lack of PLL model. It is important to consider the FFL and mathematically establish an accurate model of SOGI-PLL. Recently, the importance of frequency adaptation in the DSOGI-PLL is emphasized and analytically proved to limit the PLL dynamics by introducing a positive feedback loop [24]. However, the obtained model is rather complex and can not be directly applied to analyze the whole PLL characteristics from PLL input voltage to the grid current reference. Moreover, the abovementioned studies focus on the stability of PLL itself, but neglect the imapct of SOGI-PLL on the GCI stability in the weak grid case. Hence, in this article, the stability of both the PLL and the GCI system will be taken into account.

In order to fill this gap, this article incorporates the influence of the FFL into the modeling, and establishes the mathematical model of SOGI-PLL through harmonics linearization. The main work and contributions are summarized as follows.

1) With considering the FFL effect, a mathematical model for the SOGI-PLL is established, which is proved to be more accurate in predicting the stability of the PLL and the GCI than the aforementioned SOGI-PLL models.
2) Based on the newly-established SOGI-PLL model, the impact of parameters on the PLL itself and the GCI system is analyzed, through which the FFL's nonlinearity and the instability mechanism are clearly revealed.
3) A comprehensive and graphical design procedure for the SOGI-PLL is proposed by fully considering the stability of PLL itself, the stability of GCI, the harmonics attenuation ability, and PLL dynamics.

It is hoped that the work can lay a solid foundation for the design of PLL parameters under weak grid conditions and the further improvement for the SOGI-PLL.

II. System Description and Inverter Modeling

A. Topology and Control of the GCI

Fig. 1 illustrates the structure of a single-phase *LCL*-filtered grid-connected inverter. In Fig. 1, $U_{\rm dc}$, u_{inv}, u_g, and u_s denote

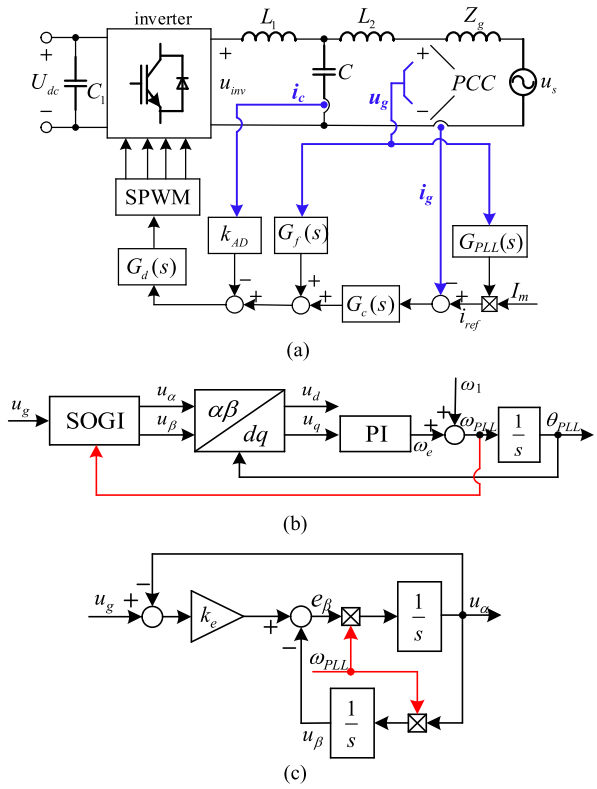

Fig. 1. Structure of single-phase *LCL*-filtered grid-connected inverter. (a) Block diagram of the GCI. (b) Structure of the SOGI-PLL. (c) Detailed scheme of the SOGI.

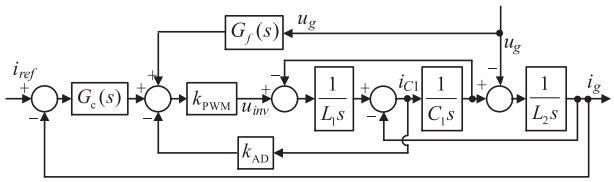

Fig. 2. Closed-loop control block diagram of the grid-connected inverter.

the dc voltage, inverter output voltage, PCC voltage, and ideal grid voltage, respectively. i_{C1} and i_g denote the capacitor current and the grid current. The inverter-side inductor L_1, capacitor C_1, and grid-side inductance L_2 together make up the *LCL* filter. Z_g is the grid impedance. I_m is the amplitude reference of i_g, and i_{ref} is the grid current reference. $G_c(s)$, $G_f(s)$, $G_d(s)$, and $G_{\rm PLL}(s)$ denote the current controller, PCC voltage feedforward, digital control delay, and PLL, separately. In this article, the SOGI-PLL is studied and its structure is shown in Fig. 1(b) and (c). $k_{\rm AD}$ is the *LCL*-filter active damping factor.

Fig. 2 depicts the GCI closed-loop control block, where $k_{\rm PWM}$ is the PWM gain with total control delay T_d. For simplifying the calculation, $|k_{\rm PWM}|$ is normalized (viewed as 1). For capacitor current active damping, the large delay is not conducive to the robustness. Hence, the delay compensation in [25] is adopted, and the total delay after compensation is about $0.5/f_s$. The used parameters of the GCI system are all given in Table I.

TABLE I
PARAMETERS OF A SINGLE-PHASE TNPC INVERTER

Parameter	Symbol	Value	Parameter	Symbol	Value
Rated power	P_{rated}	5 kW	Inverter-side inductance	L_1	0.75mH
DC voltage	U_{dc}	760 V	Grid-side inductance	L_2	0.45mH
Grid voltage	U_g U_{gm}	220 V 311 V	Filter capacitance	C_1	6.8 μF
Grid frequency	ω_1	100π rad/s	Switching frequency	f_{sw}	15 kHz
PR current controller	k_p, k_r, ω_c	9, 600, 6	Sampling frequency	f_s	15 kHz
PCC voltage feedforward	$G_f(s)$	0.6	Total delay	T_d	0.5/f_s
Active damping	k_{AD}	13			

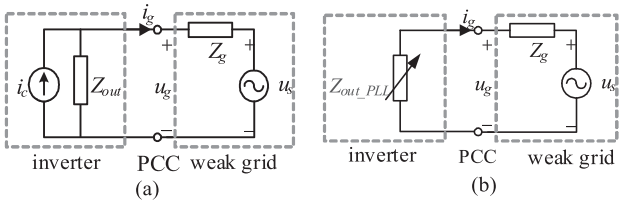

Fig. 3. Impedance model of the grid-connected system. (a) Typical Norton model. (b) Revised model considering the PLL effect.

B. Impedance Model of the GCI

Fig. 3(a) shows the inverter output impedance model without considering the influence of the PLL [26], where the inverter is regarded as a current source i_c (controlled by i_{ref}) in parallel with its output impedance Z_{out}, and the grid can be approximately replaced by the voltage source u_s in series with grid impedance Z_g. However, the grid current reference i_{ref} and the PCC voltage u_g are coupled by the PLL, i.e., $i_{ref}(s) = I_m G_{\text{PLL}}(s) u_g(s)$. Hence, the inverter output impedance should be revised as [3]

$$Z_{\text{out\_PLL}}(s) = \frac{\left[\begin{array}{l} L_1L_2C_1s^3 + k_{\text{AD}}k_{\text{PWM}}L_2C_1s^2 + (L_1+L_2)s \\ \quad + G_c(s)k_{\text{PWM}} \end{array}\right]}{\left[\begin{array}{l} L_1C_1s^2 + k_{\text{AD}}k_{\text{PWM}}C_1s + 1 - G_f(s)k_{\text{PWM}} \\ \quad - I_m G_{\text{PLL}}(s)G_c(s)k_{\text{PWM}} \end{array}\right]}. \tag{1}$$

The output impedance model can be transformed into the one in Fig. 3(b). Following the impedance stability criterion in [26], the GCI stability is easily predicted by applying the Nyquist stability criterion to the impedance ratio Z_g / $Z_{\text{out·PLL}}$. It is easy to know that, in order to precisely analyze the system stability, an accurate model for the SOGI-PLL must be obtained. But, as mentioned in Section I, the frequency feedback loop is usually ignored, yielding an inaccurate model. Fig. 4 presents the simulation results of the SOGI-PLL. Clearly, other than the dominant dc component, certain amount of 100 Hz component exists in ω_{PLL} as well. In the following, it will be shown that how the PLL behavior and GCI stability are affected by such component that neglected in the previous work.

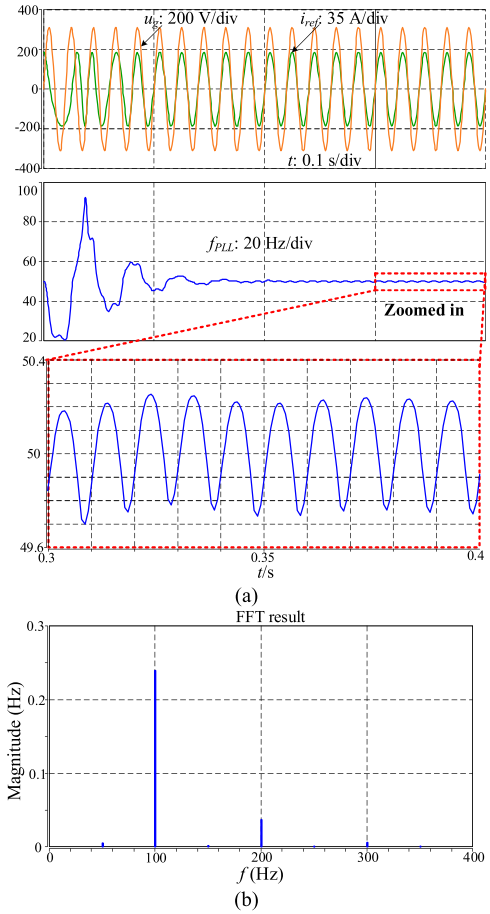

Fig. 4. Simulation results of the SOGI-PLL. (a) u_g, i_{ref}, and f_{PLL}. (b) FFT result of ω_{PLL}.

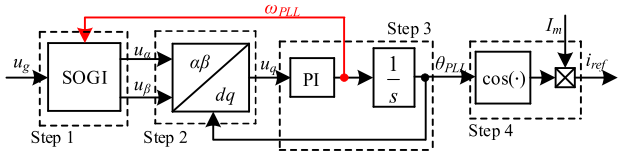

Fig. 5. Modeling procedure for the SOGI-PLL.

III. SOGI-PLL Modeling and Validations

In this section, as shown in Fig. 5, the SOGI-PLL is divided into four parts for obtaining an intuitive and accurate model.

Step 1: Establish the model of the SOGI, where the input is u_g, ω_{PLL} and the output is u_α, u_β.
Step 2: Establish the model of the Park transformation, where the input is u_α and u_β and the output is u_q.
Step 3: Establish the model of the SRF-PLL, where the input is u_q and the output is θ_{PLL}.
Step 4: Establish the model of the grid current reference reconstruction, where the input is θ_{PLL} and the output is i_{ref}.

Step 1. SOGI module modeling: When a disturbance signal at frequency f_p is injected into the GCI, the component with the frequency of $mf_p \pm nf_1$ ($m \in N$, $n \in N$) will be generated [22], [27]. To perform linearization in the modeling process, the dominant frequency component of $f_p \pm nf_1$ ($n \in N$) is usually considered and $m = 1$ is taken. In terms of the frequency spectrum of each response component, each ac variable mainly contains the frequency component of $f_p \pm nf_1$ ($n = 1, 3, 5, ...$) and each dc variable mainly contains the frequency component at $f_p \pm nf_1$ ($n = 0, 2, 4, ...$). The larger the coefficient n is, the smaller the proportion or amplitude of this frequency component is [28]. Therefore, in this article, the ac variables (e.g., u_g, u_α, u_β) only considers the component at $f_p \pm f_1$. Here, define $f_p + f_1$ as "positive mirror frequency" and define $f_p - f_1$ as "negative mirror frequency". For the dc variables in the SOGI-PLL (e.g., u_d, u_q, ω_{PLL}), only the component at f_p is considered. Note that the feasibility of dominant components selection will be validated at the end of this section.

According to the abovementioned analysis, the PLL input voltage u_g is

$$u_g(t) = U_{gm}\cos(2\pi f_1 t) + U_p\cos[2\pi(f_p + f_1)t + \varphi_{vp}] + U_n\cos[2\pi(f_p - f_1)t + \varphi_{vn}] \quad (2)$$

where U_{gm} is the amplitude of the fundamental voltage at f_1, U_p and φ_{vp} are the amplitude and initial phase of "positive mirror frequency" voltage at $f_p + f_1$, and U_n and φ_{vn} are the amplitude and initial phase of the "negative mirror frequency" voltage at f_p - f_1. Other symbols in the article follow the same notation.

The Fourier coefficient for u_g in (2) is

$$U_g[f] = \begin{cases} \frac{U_{gm}}{2}, f = \pm f_1 \\ \frac{U_p}{2}e^{\pm j\varphi_{vp}}, f = \pm(f_p + f_1) \\ \frac{U_n}{2}e^{\pm j\varphi_{vn}}, f = \pm(f_p - f_1). \end{cases} \quad (3)$$

Similarly, assume the time-domain expression for u_α, u_β, and ω_{PLL} to be

$$u_\alpha(t) = U_{gm}\cos(2\pi f_1 t) + U_{\alpha p}\cos[2\pi(f_p + f_1)t + \varphi_{\alpha p}] + U_{\alpha n}\cos[2\pi(f_p - f_1)t + \varphi_{\alpha n}] \quad (4)$$

$$u_\beta(t) = U_{gm}\sin(2\pi f_1 t) + U_{\beta p}\cos[2\pi(f_p + f_1)t + \varphi_{\beta p}] + U_{\beta n}\cos[2\pi(f_p - f_1)t + \varphi_{\beta n}] \quad (5)$$

$$\omega_{\mathrm{PLL}}(t) = \omega_1 + \Omega_s\cos(2\pi f_p t + \varphi_{\omega s}). \quad (6)$$

The Fourier coefficients for u_α, u_β, and ω_{PLL} are

$$U_\alpha[f] = \begin{cases} \frac{U_{gm}}{2}, f = \pm f_1 \\ \boldsymbol{V_{\alpha p}}, f = \pm(f_p + f_1) \\ \boldsymbol{V_{\alpha n}}, f = \pm(f_p - f_1) \end{cases} \quad (7)$$

$$U_\beta[f] = \begin{cases} \pm\frac{U_{gm}}{2j}, f = \pm f_1 \\ \boldsymbol{V_{\beta p}}, f = \pm(f_p + f_1) \\ \boldsymbol{V_{\beta n}}, f = \pm(f_p - f_1) \end{cases} \quad (8)$$

$$\Omega_{PLL}[f] = \begin{cases} \omega_1, f = 0 \\ \boldsymbol{\Omega_s}, f = \pm f_p \end{cases} \quad (9)$$

where $\boldsymbol{V_{\alpha p}} = \frac{U_{\alpha p}}{2}e^{\pm j\varphi_{\alpha p}}$, and the rest of Fourier coefficients $\boldsymbol{V_{\alpha n}}$, $\boldsymbol{V_{\beta p}}$, $\boldsymbol{V_{\beta n}}$, and Ω_s follow similar shorthand notations.

For the SOGI, there are two inputs: one is u_g and the other is the estimated angular frequency ω_{PLL} (reflecting the frequency feedback loop). For the cross-product value of the disturbance components in u_g and ω_{PLL} is small, the frequency responses of u_α and u_β with respect to u_g and ω_{PLL} are calculated separately.

A. Transfer Functions From ω_{PLL} to u_α, U_β

Usually, in the past, ω_{PLL} is viewed as its steady-state value of about 314 rad/s. In this article, the influence of disturbance in ω_{PLL} on u_α and u_β is taken into account. Hence, u_g is viewed as its fundamental component without any disturbance but ω_{PLL} is viewed, as shown in (9).

Based on Fig. 1(c), the time-domain expression of e_β is

$$e_\beta = k_e(u_g - u_\alpha) - u_\beta. \quad (10)$$

And the frequency-domain expression of e_β is

$$E_\beta[f] = \begin{cases} \pm j\frac{U_{gm}}{2}, f = \pm f_1 \\ -(k_e\boldsymbol{V_{\alpha p}} + \boldsymbol{V_{\beta p}}), f = \pm(f_p + f_1) \\ -(k_e\boldsymbol{V_{\alpha n}} + \boldsymbol{V_{\beta n}}), f = \pm(f_p - f_1). \end{cases} \quad (11)$$

Based on Fig. 1(c), the time-domain expression of u_α and u_β is

$$u_\alpha = \int(e_\beta \times \omega_{\mathrm{PLL}})dt \quad (12)$$

$$u_\beta = \int(u_\alpha \times \omega_{\mathrm{PLL}})dt. \quad (13)$$

Substituting (11) into the frequency-domain expression of (12) and (13), it has

$$\boldsymbol{V_{\alpha p}} = \frac{1}{2\pi(f_p + f_1)} \times \left[\frac{U_{gm}}{2}\boldsymbol{\Omega_s} + j\omega_1(k_e\boldsymbol{V_{\alpha p}} + \boldsymbol{V_{\beta p}})\right] \quad (14)$$

$$\boldsymbol{V_{\beta p}} = -\frac{jU_{gm}\boldsymbol{\Omega_s}}{2\omega_1} + \frac{\omega_1^2(k_e\boldsymbol{V_{\alpha p}} + \boldsymbol{V_{\beta p}}) - \frac{j\omega_1 U_{gm}\boldsymbol{\Omega_s}}{2}}{[2\pi(f_p + f_1)]^2}. \quad (15)$$

By comparing the coefficients of (14)–(15) with (7)–(8), the gain from ω_{PLL} to u_α and u_β at "positive mirror frequency" can be obtained and expressed as

$$P_\alpha(s) = \frac{u_\alpha(s + j\omega_1)}{\Omega_{PLL}(s)} = -\frac{U_{gm}}{jk_e\omega_1}G_\alpha(s + j\omega_1) \quad (16)$$

$$P_\beta(s) = \frac{u_\beta(s + j\omega_1)}{\Omega_{PLL}(s)} = -\frac{U_{gm}}{jk_e\omega_1}G_\beta(s + j\omega_1) + \frac{U_{gm}}{j2\omega_1}. \quad (17)$$

The transfer function at the "negative mirror frequency" can also be obtained as

$$N_\alpha(s) = \frac{u_\alpha(s - j\omega_1)}{\Omega_{PLL}(s)} = \frac{U_{gm}}{jk_e\omega_1}G_\alpha(s - j\omega_1) \quad (18)$$

$$N_\beta(s) = \frac{u_\beta(s - j\omega_1)}{\Omega_{\mathrm{PLL}}(s)} = \frac{U_{gm}}{jk_e\omega_1}G_\beta(s - j\omega_1) - \frac{U_{gm}}{j2\omega_1}. \quad (19)$$

B. Transfer Functions From U_g to u_α, U_β

In Fig. 1(c), neglecting the disturbance influence of $\omega_{\rm PLL}$ and according to the Mason's formula, it is easy to obtain that

$$G_\alpha(s)=\frac{u_\alpha(s)}{u_g(s)}=\frac{k_e\omega_1 s}{s^2+k_e\omega_1 s+\omega_1^2} \tag{20}$$

$$G_\beta(s)=\frac{u_\beta(s)}{u_g(s)}=\frac{k_e\omega_1^2}{s^2+k_e\omega_1 s+\omega_1^2}. \tag{21}$$

Combining (16)–(21) together, gives

$$\begin{aligned} u_\alpha(s+j\omega_1)&=P_\alpha(s)\Omega_{\rm PLL}(s)\\ &\quad+G_\alpha(s+j\omega_1)u_g(s+j\omega_1) \end{aligned} \tag{22}$$

$$\begin{aligned} u_\beta(s+j\omega_1)&=P_\beta(s)\Omega_{\rm PLL}(s)\\ &\quad+G_\beta(s+j\omega_1)u_g(s+j\omega_1) \end{aligned} \tag{23}$$

$$\begin{aligned} u_\alpha(s-j\omega_1)&=N_\alpha(s)\Omega_{\rm PLL}(s)\\ &\quad+G_\alpha(s-j\omega_1)u_g(s-j\omega_1) \end{aligned} \tag{24}$$

$$\begin{aligned} u_\beta(s-j\omega_1)&=N_\beta(s)\Omega_{\rm PLL}(s)\\ &\quad+G_\beta(s-j\omega_1)u_g(s-j\omega_1). \end{aligned} \tag{25}$$

Hence, the modeling of the SOGI is completed.

Step 2. Park transformation module modeling: The time-domain expression of the Park transformation is

$$\begin{aligned} \begin{bmatrix} u_d\\ u_q\end{bmatrix}&=\begin{bmatrix}\cos\theta_{\rm PLL} & \sin\theta_{\rm PLL}\\ -\sin\theta_{\rm PLL} & \cos\theta_{\rm PLL}\end{bmatrix}\cdot\begin{bmatrix}u_\alpha\\ u_\beta\end{bmatrix}\\ &=T_{\alpha\beta\to dq}(\theta_{\rm PLL})\cdot\begin{bmatrix}u_\alpha\\ u_\beta\end{bmatrix}. \end{aligned} \tag{26}$$

If the input voltage has no disturbance, the corresponding PLL estimated phase angle is denoted as θ_1. However, when the influence of input voltage disturbance is taken into account, an angle difference (denoted as $\Delta\theta$) between the estimated phase angle $\theta_{\rm PLL}$ and θ_1 appears, i.e.,

$$\theta_{\rm PLL}=\theta_1+\Delta\theta. \tag{27}$$

Substituting (27) into (26), $T_{\alpha\beta\to dq}(\theta_{\rm PLL})$ can be rewritten as

$$T_{\alpha\beta\to dq}(\theta_{\rm PLL})=T_{\alpha\beta\to dq}(\Delta\theta)\cdot T_{\alpha\beta\to dq}(\theta_1). \tag{28}$$

Note that all the variables after the product of u_d, u_q and $T_{\alpha\beta\to dq}(\theta_1)$ are labelled with the corresponding subscripts of "v". Combining (26)–(28), it can be obtained that

$$u_{dv}+ju_{qv}=(u_\alpha+ju_\beta)e^{-j\omega_1 t}. \tag{29}$$

Notice that the quadratic term in the disturbance component has been omitted in (29). And, it can be seen from (29) that u_{qv} contains components with frequencies of f_p, $f_p\pm 2f_1$, and so on. On the one hand, $f_p\pm 2f_1$ and other frequency components are relatively small; On the other hand, $f_p\pm 2f_1$ and other frequency components did not contribute to the final single-input-single-output model of PLL [29]. Hence, only the component at f_p is considered in u_{qv}, which gives

$$U_{qv}[f]\,\big|_{f=f_p}=\frac{\boldsymbol{V_{\alpha p}}-\boldsymbol{V_{\alpha n}}}{2j}+\frac{\boldsymbol{V_{\beta p}}+\boldsymbol{V_{\beta n}}}{2}. \tag{30}$$

Rewriting (30) in the form of a transfer function, yields

$$\begin{aligned} u_{qv}(s)=&-\frac{u_\alpha(s-j\omega_1)-u_\alpha(s+j\omega_1)}{2j}\\ &+\frac{u_\beta(s-j\omega_1)-u_\beta(s+j\omega_1)}{2}. \end{aligned} \tag{31}$$

Then, the modeling of Park transformation is completed.

Step 3. SRF-PLL module modeling: Harmonic linearization modeling of the SRF-PLL has been described in detail in many past studies like [21], [22], [29]. The corresponding transfer function is given directly without further elaboration here, i.e.,

$$\begin{aligned} \Delta\theta(s)&=\frac{\left(k_{p\_pll}+\frac{k_{i\_pll}}{s}\right)\cdot\frac{1}{s}}{1+U_{gm}\left(k_{p\_pll}+\frac{k_{i\_pll}}{s}\right)\cdot\frac{1}{s}}\cdot u_{qv}(s)\\ &=T_{\rm PLL}(s)\cdot u_{qv}(s) \end{aligned} \tag{32}$$

where k_{p_pll} and k_{i_pll} are the proportional coefficient and integral coefficient of PI regulator of PLL, respectively.

Step 4. Current reference reconstruction module modeling: According to Fig. 1(c), the time-domain expression of i_{ref} is

$$i_{ref}=I_m\cos\theta_{\rm PLL}. \tag{33}$$

Substituting (27) into (33), gives

$$\begin{aligned} i_{ref}&=I_m\cos(\theta_1+\Delta\theta)\\ &\approx I_m\cos\theta_1-I_m\Delta\theta\sin\theta_1\\ &=I_{ref}+i_{ref\_v}. \end{aligned} \tag{34}$$

Applying the Laplace transform to i_{ref_v}, yields

$$i_{ref\_v}(s)=-\frac{I_m}{2j}[\Delta\theta(s-j\omega_1)-\Delta\theta(s+j\omega_1)]. \tag{35}$$

Modeling of current reference reconstruction is completed.

At last, combine the modeling results in Steps 1–4, the desired transfer function of the SOGI-PLL is

$$G_{\rm SOGI-PLL}(s)=-\frac{1}{2j}[G_p(s-j\omega_1)-G_n(s+j\omega_1)] \tag{36}$$

$$G_p(s)=\frac{T_{\rm PLL}(s)\cdot[-jG_\alpha(s+j\omega_1)+G_\beta(s+j\omega_1)]}{2-sT_{\rm PLL}(s)\cdot[-jP_\alpha(s)+jN_\alpha(s)+P_\beta(s)+N_\beta(s)]} \tag{37}$$

$$G_n(s)=\frac{T_{\rm PLL}(s)\cdot[jG_\alpha(s-j\omega_1)+G_\beta(s-j\omega_1)]}{2-sT_{\rm PLL}(s)\cdot[-jP_\alpha(s)+jN_\alpha(s)+P_\beta(s)+N_\beta(s)]} \tag{38}$$

where the transfer functions of $G_p(s)$ and $G_n(s)$ are depicted at the bottom of this page.

TABLE II
COMPARISON OF DIFFERENT MODELING METHODS FOR THE SOGI-PLL

	LTI/LTP	FFL considered?	DC gain prediction	Low-frequency accuracy	Model complexity
Model-1	LTI	No	High	Low	Simple
Model-2	LTP	No	Low	Medium	Simple
Model-3	LTP	No	Relatively high	Medium	Medium
Proposed	LTP	Yes	High	High	Medium

*LTI and LTP represent 'linear time-invariant' and 'linear time-periodic' modeling.

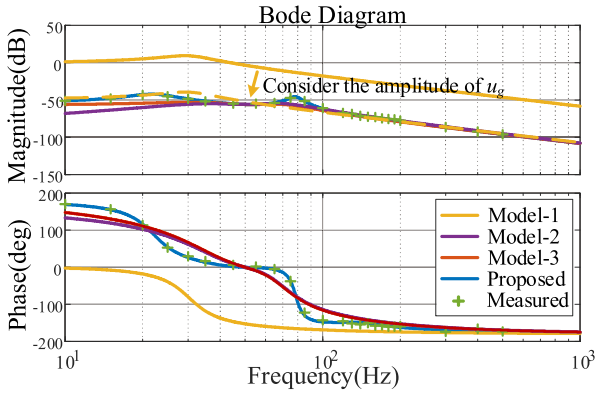

Fig. 6. Bode plots of proposed theoretical model and simulation measurements for the SOGI-PLL.

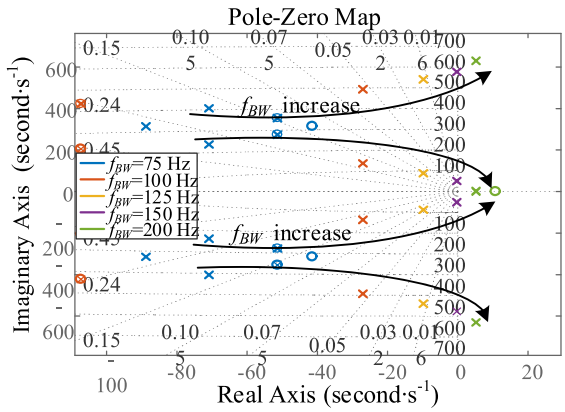

Fig. 7. Pole-zero map of the SOGI-PLL under different f_{BW}.

To verify the accuracy of the proposed mathematical model shown in (36), a simulation model of the SOGI-PLL was built in MATLAB/Simulink. By injecting a disturbance with 4% amplitude of the fundamental grid voltage into the input voltage u_g, the FFT function provided by the "powergui" module in Simulink is used to detect the amplitude and phase of relevant frequency components in i_{ref} point by point. During this test, the SOGI-PLL parameters are $k_e = 1.414$, $k_{p\_pll} = 0.69$, and $k_{i\_pll} = 75$. Fig. 6 shows the Bode diagrams of the measured results and the theoretical model results. In order to show the benefit of the proposed model, Model-1 in [19], Model-2 in [20], and Model-3 in [21], [22] are drawn together in Fig. 6.

It can be seen and concluded from Fig. 6 that as follows.

1) The measured results are very consistent with the proposed SOGI-PLL theoretical model, which proves the correctness of the newly-established model as well as the reasonable selection of dominant frequency components as mentioned at the beginning of Step 1.
2) Model-1 actually reflects the transfer function from the input phase angle to the output phase angle (i.e., from θ_g to θ_{PLL}) and thus cannot reflect the frequency characteristics of the SOGI-PLL. If the amplitude influence of u_g is taken into account (as shown by the orange dotted line in Fig. 6), the revised amplitude-frequency curve of model 1 is much closer to the measured one, but it still cannot reflect the resonant peak in the amplitude-frequency curve (above the fundamental frequency), and the phase mismatch is large.
3) The Bode diagrams of Models 2 and 3 are consistent with the measurement results above 200 Hz, but there still exists considerably large mismatch below 200 Hz.
4) In conclusion, compared with existing Models 1, 2, and 3, the proposed model is more accurate and can better reflect the actual frequency characteristics of the SOGI-PLL.

A comparison of the differences among Model-1, Model-2, Model-3, and the proposed model is summarized in Table II.

IV. IMPACT OF SOGI-PLL PARAMETERS ON THE PLL ITSELF AND THE GCI

A. Traditional Design Guideline

In [19], a design method for the three control parameters of the SOGI-PLL is comprehensively considered, but this method is relatively complex. Then, in [20], based on a simple model, the SOGI parameter (k_e) and PI parameters (k_{p_pll} and k_{i_pll}) can be designed separately. Considering the harmonic suppression ability and dynamic performance, a compromise is taken that k_e is selected as 1.414 [11], [15]. In the following, k_e is set as 1.414 if not specified. For k_{p_pll} and k_{i_pll}, they are usually determined by the damping factor ξ and PLL bandwidth f_{BW} from a typical second-order system model proposed in [20]. Generally, ξ is set as 0.707, which is an optimum value for the overshoot and the settling time. Therefore, according to the traditional PLL design method in [20], the SOGI-PLL parameters are determined only by the bandwidth of SRF-PLL part.

B. Impact of SRF-PLL Bandwidth on SOGI-PLL and GCI

It should be pointed out that the SOGI-PLL behaves strong nonlinearity, which means its bandwidth should not be too large, otherwise the PLL itself will become unstable. Fig. 7 shows the

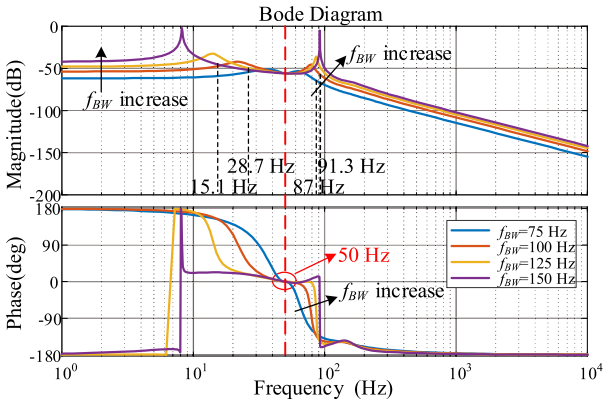

Fig. 8. Bode plots of the SOGI-PLL under different f_{BW} of SRF-PLL part.

pole-zero maps of SOGI-PLL with $k_e = 1.414$ for different SRF-PLL bandwidth. Seen from Fig. 7, when f_{BW} increases, two pairs of dominant poles gradually move from the left half-plane to the right half-plane, indicating the instability of the SOGI-PLL.

In [30], it is pointed out that the SOGI-PLL is approximately regarded as the cascade of SOGI and SRF-PLL in the case of a small PLL bandwidth. In other words, the bandwidth of the overall PLL system is also affected by the SOGI. To compare the relationship between the actual bandwidth of SOGI-PLL and the bandwidth of SRF-PLL, Fig. 8 shows the Bode diagram of SOGI-PLL when the bandwidth of SRF-PLL part is 75, 100, 125, and 150 Hz, respectively. As can be seen from Fig. 8, the PLL bandwidth decreases sharply with the increase of f_{BW}, and the two resonant peaks become much more prominent in the amplitude-frequency curve. This indicates that the nonlinear impact of SOGI-PLL becomes more obvious with the increase of f_{BW}. In other words, the influence of frequency feedback loop on the PLL frequency characteristics is more significant when f_{BW} turns larger. Note that the gain and phase angle around 50 Hz are never changed, which is a necessary property for the phase locking mission of the PLL.

Then, the main effects of the frequency feedback loop are summarized as follows.

1) The two resonant peaks become much larger and their frequencies change along the 50 Hz line to both sides.
2) The loop gain of the PLL moves up and the PLL bandwidth decreases mainly due to the increase of dc gain.

It is worth noting that Fig. 8 shows that the dc gain of the PLL increases with the increase of f_{BW}. That is, the suppression of dc offset in the grid voltage will be affected by the increase of f_{BW}, which is quite different from the dc characteristics reflected by the models proposed earlier (e.g., models 1–3).

Table III shows the dc current value of the SOGI-PLL under different SRF-PLL bandwidths, obtained from Simulations. It can be seen from Table III that the theoretically-calculated value of the SOGI-PLL dc gain is close to the measured value and increases with the increase of f_{BW}, which verifies the theoretical analysis. Note that the SOGI-PLL cannot work stably at 150 Hz, which corresponds to the dominant poles in Fig. 7 located near the imaginary axis.

TABLE III
DC GAIN OF THE SOGI-PLL WITH DIFFERENT f_{BW}

f_{BW} (Hz)	dc input (V)	dc output (A)	
		theoretical	measured
75	10	0.26	0.27
100	10	0.75	0.75
150	10	unstable	

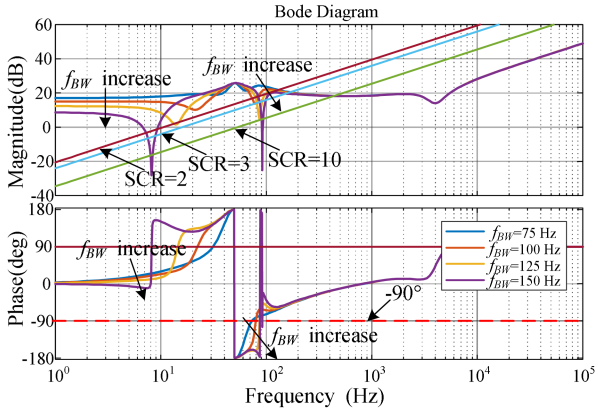

Fig. 9. Bode plots of the inverter output impedance under different f_{BW}.

By substituting the proposed SOGI-PLL model into (1), the stability of overall GCI system is then evaluated. Fig. 9 shows some Bode plots of inverter output impedance $Z_{\mathrm{out\_PLL}}$ when the short-circuit ratio (SCR) is 2, 3, 10 and the SRF-PLL bandwidth is 75, 100, 125, 150 Hz, respectively. When f_{BW} increases, the frequency at the intersection of $Z_{\mathrm{out\_PLL}}$ and Z_g in the amplitude-frequency curve grows gradually but the phase margin of the inverter system decreases. When f_{BW} increases to 150 Hz, even if SCR is 10 (Z_g is small), the phase at the intersection frequency is below $-90°$ and the inverter system is unstable. In this case, $Z_{\mathrm{out\_PLL}}$ and Z_g intersect between 80–100 Hz (i.e., the frequency around the second resonant peak in Fig. 8, as revealed by the proposed SOGI-PLL model), where the phase-frequency curve changes dramatically.

C. Impact of SOGI Parameter $\mathrm{K_e}$

It has been mentioned that $k_e = 1.414$ is generally considered in previous literature. In fact, known from the transfer function of SOGI-PLL [as shown in (36)], the influence of k_e should not be ignored. Fig. 10 shows the influence of different k_e values on SOGI-PLL when the bandwidth of SRF-PLL part is set at 100 Hz. With the increase of k_e, the resonant peak in the amplitude-frequency curve is suppressed, but the rejection ability at higher frequencies is weakened. Another advantage of larger k_e is the faster dynamics of the SOGI and, thus, the whole SOGI-PLL.

Fig. 11 shows the Bode diagram of $Z_{\mathrm{out\_PLL}}$ under different k_e when the SRF-PLL bandwidth is 100 Hz. In the figure, with k_e increasing, the notch at the resonant peak frequency of SOGI-PLL gradually moves up, and finally there does not exist the

TABLE IV
PLL PARAMETERS EFFECTS ON THE SOGI-PLL AND GCI WITH/WITHOUT CONSIDERING THE FFL EFFECT

Parameter	Without considering the FFL		Considering the FFL	
	Effect on SOGI-PLL itself	Effect on the GCI	Effect on SOGI-PLL itself	Effect on the GCI
Increasing k_e	➢ Fasten the dynamics ➢ Weaken the harmonics attenuation	➢ Little effect on the GCI stability	➢ Reduce the resonant peak caused by FFL ➢ Help improve the stability ➢ Fasten the dynamics ➢ Weaken the harmonics attenuation	➢ Reduce the resonant peak caused by FFL ➢ Help improve the stability
Increasing f_{BW}	➢ Slightly affect the stability (due to the failure of resonant peak prediction) ➢ Do not affect the dc gain	➢ Weaken the stability (normally due to the coupling of current loop and PLL)	➢ Increase the resonant peak caused by FFL ➢ Weaken the stability ➢ Reduce the whole PLL bandwidth ➢ Increase the dc gain	➢ Increase the resonant peak caused by FFL ➢ Weaken the stability more seriously due to the resonant peak

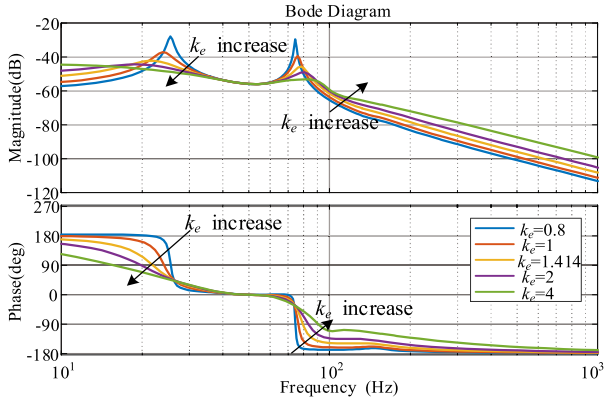

Fig. 10. Bode plots of the SOGI-PLL while k_e takes different values.

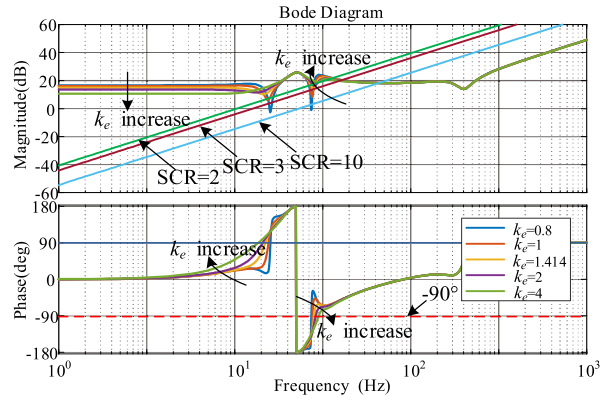

Fig. 11. Bode plots of the inverter output impedance while k_e takes different values.

intersection for SCR = 3 and $k_e = 1.414$, meaning that increasing k_e can improve the stability of the GCI system under the weak grid condition. However, increasing k_e will weaken the filtering ability of the SOGI, and then affects the estimation accuracy of the PLL. Therefore, for k_e, a compromise has to be made by considering both the PLL estimation accuracy and weak grid robustness.

At last, by considering the inherent frequency loop coupling, the effects of PLL parameters on the SOGI-PLL itself and the GCI stability are summarized in Table IV. For the purpose of comparison, the results of ignoring the FFL are also given.

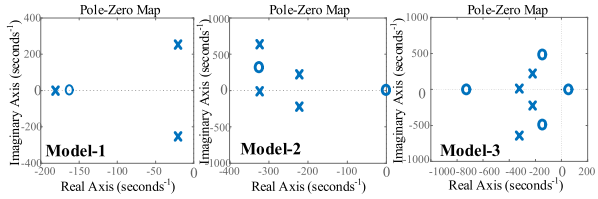

Fig. 12. Pole-zero map of the SOGI-PLL with different models under $k_e = 1.414$, $f_{\mathrm{BW}} = 200$ Hz.

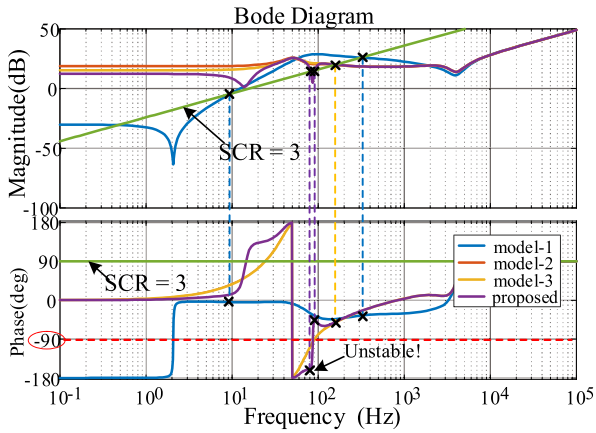

Fig. 13. Bode plot of the inverter output impedance under $k_e = 1.414$, $f_{\mathrm{BW}} = 150$ Hz, with grid impedance $L_g = 10$ mH (corresponding to SCR = 3).

D. Comparisons of Different SOGI-PLL Models

Fig. 12 shows the pole-zero maps of different SOGI-PLL models under $k_e = 1.414$, $f_{\mathrm{BW}} = 200$ Hz (denoted as Case I). Compared with the proposed model (see Fig. 7 for $f_{\mathrm{BW}} = 200$ Hz), the existing models all fail to predict the right half-plane poles in the SOGI-PLL under Case I.

Fig. 13 shows the Bode plots of Z_g and $Z_{\mathrm{out\_PLL}}$ with using different SOGI-PLL models under $k_e = 1.414$, $f_{\mathrm{BW}} = 150$ Hz and $L_g = 10$ mH (denoted as Case II). The proposed model reveals that $Z_{\mathrm{out\_PLL}}$ and Z_g intersect at a frequency where the

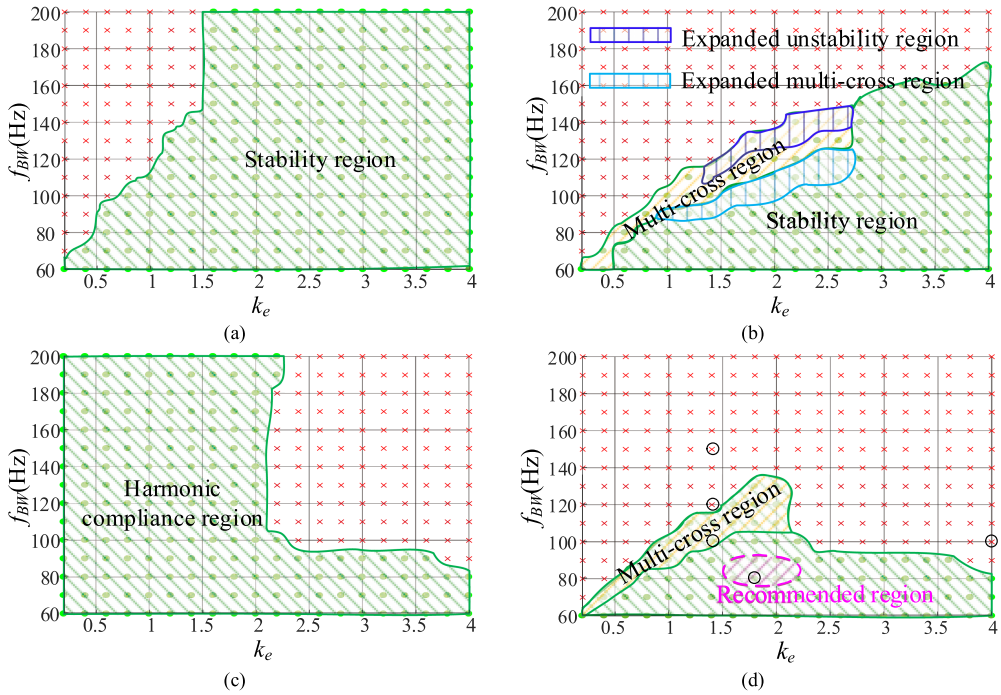

Fig. 14. Optional parameter region of the SOGI-PLL. (a) Consider the PLL stability only. (b) Consider the GCI stability and the variation of L_g from 10–15 mH. (c) Consider the PLL harmonic attenuation only. (d) Consider all the factors in (a)–(c) where L_g is set as 15 mH.

phase of $Z_{\text{out\_PLL}}$ is much below $-90°$, meaning that the GCI is unstable. However, the rest models fail to predict the instability of the GCI under Case II.

V. Proposed Parameters Design of SOGI-PLL

The considered control performance includes three aspects: 1) stability, 2) accuracy, and 3) rapidity. The "stability" requires that the PLL must first ensure its own stable operation, the "accuracy" means that the PLL must be able to synchronize with the PCC voltage under various conditions, and the "rapidity" means that the PLL should track the phase and fundamental frequency of PCC voltage quickly. In addition, the GCI stability should be also considered under the weak grid. To sum up, in this section, the following factors are guaranteed by the parameters design:

1) stability of the SOGI-PLL itself;
2) stability of the GCI under the weak grid;
3) accurate estimation under voltage harmonics;
4) desired transient response (not too slow).

Firstly, the stability of SOGI-PLL itself is considered. By using the SOGI-PLL transfer function deduced in Section III and the MATLAB function "isstable()", the stability of SOGI-PLL with different k_e and SRF-PLL bandwidth f_{BW} is judged, as shown in Fig. 14(a) . Seen from Fig. 14(a), too small k_e or large f_{BW} leads to the instability of PLL itself. In addition, the smaller the parameter k_e is, the smaller the SRF-PLL bandwidth f_{BW} will be, in the premise of ensuring the stability of SOGI-PLL itself. When k_e reaches a certain value [about 1.5 in Fig. 14(a)], it can be guaranteed that the PLL itself is basically stable.

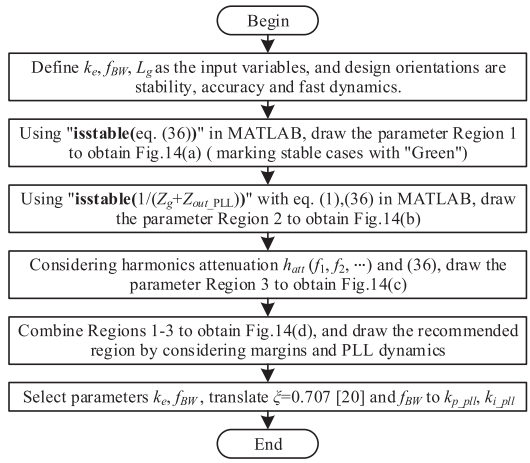

Fig. 15. Proposed design procedure for the SOGI-PLL.

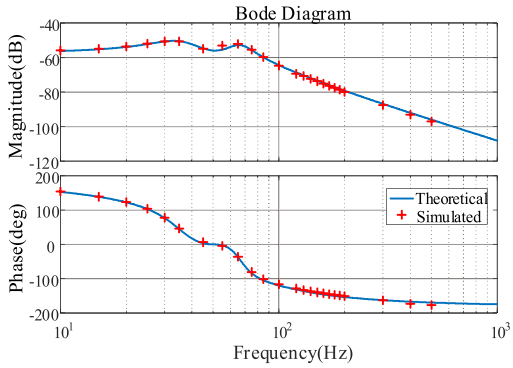

Fig. 16. Bode plots of the LPF-SOGI-PLL.

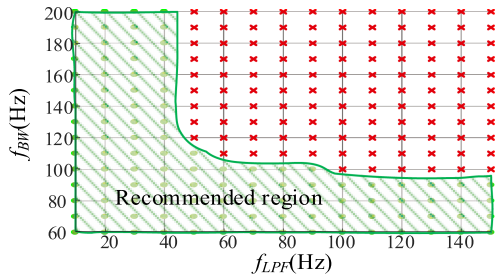

Fig. 17. Optional parameter range of the LPF-SOGI-PLL.

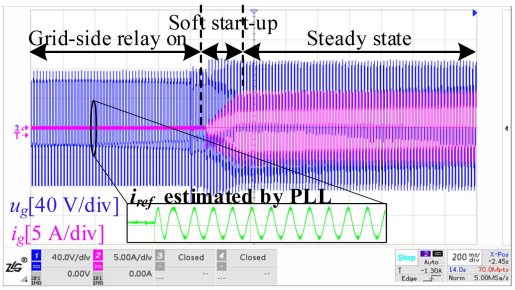

Fig. 18. Start-up waveforms of the GCI.

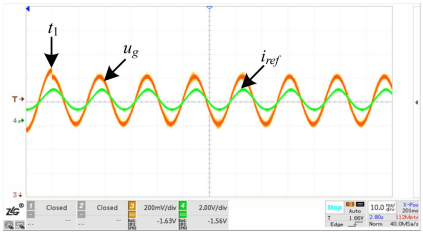

(a)

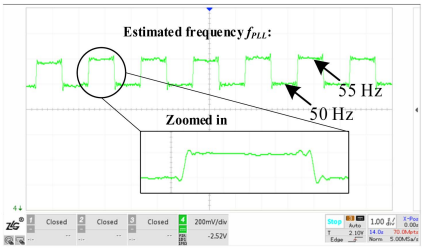

(b)

u_g	f / Hz	Amplitude / V	Phase / rad	f_{PLL}	f / Hz	Amplitude / V	Phase / rad
频率/Hz		幅值/V	相位/r	频率/Hz		幅值/V	相位/r
0	DC	1.70	---	0	DC	2.81	---
1	50.00	239m	0.60	1	50.00	434m	0.78
2	1.269M	3.50m	2.34	2	100.0	186m	-0.16
3	100.0	2.48m	-2.59	3	200.0	37.9m	-2.11
4	1.588M	2.15m	-0.64	4	250.0	26.6m	-2.11
5	634.6k	1.91m	-2.61	5	150.0	20.3m	-1.33
6	150.0	1.63m	1.80	6	300.0	14.6m	-2.06
7	1.269M	1.34m	-2.11	7	26.47	12.5m	-2.17
8	1.269M	1.32m	0.97	8	23.53	12.2m	0.46
9	250.0	1.27m	2.98	9	35.29	11.7m	-1.22
10	2.223M	1.20m	-2.05	10	38.24	7.51m	-2.00

(c)

Fig. 19. Frequency response results of the SOGI-PLL under a frequency jump. (a) u_g and i_{ref}. (b) Estimated frequency f_{PLL}. (c) FFT result of u_g and unfiltered f_{PLL}.

TABLE V
ACCURACY OF DIFFERENT MODELS FOR SPECIFIC CASES

Stability results		Case I	Case II
Theoretical predictions	Model-1	Stable	Stable
	Model-2	Stable	Stable
	Model-3	Stable	Stable
	Proposed	Unstable	Unstable
Experimental records		Unstable	Unstable

Similarly, using the SOGI-PLL mathematical model and the impedance stability criterion, the influence of PLL parameters on the stability of the inverter under weak grids can be analyzed. Fig. 14(b) shows the optional range of parameters considering the GCI stability in the weak grid (first, take $L_g = 10$ mH for analysis as the basis). Compared with Fig. 14(a), the optional parameter range in Fig. 14(b) is somewhat narrowed, which is mainly caused by negative resistance characteristics of PLL and nonlinear coupling of SOGI-PLL. Note that the multicrossing region (where the output impedance and the grid impedance intersect at multifrequencies) is not recommended. When L_g increases from 10–15 mH, the optional area will be further reduced [see the expanded region in Fig. 14(b)].

In addition to the PLL stability and the GCI stability, the harmonic suppression of PLL itself should also be considered. In [31], it is revealed that typical odd harmonics in the grid should be suppressed with $[-20, -40]$ dB. Considering that the mathematical model in [31] is the relation from phase angle to phase angle, the constraint should be divided by the amplitude of the PCC voltage when considering the voltage as the input. Therefore, two points are considered here: 1) suppress the odd harmonics below -70 dB; 2) suppress the resonant peak (caused by the frequency feedback loop in the PLL) below -50 dB to prevent amplifying the low-frequency inter-harmonics.

Fig. 14(c) shows the optional parameter region considering the harmonics suppression capability. According to Fig. 14(c), when k_e or SRF-PLL bandwidth f_{BW} is too large, the harmonic suppression of PLL does not meet the requirements. In practical application, if the voltage harmonics at PCC are too large or the phase-locking accuracy is required to be higher, the constraint shall be further restrained [32]. Anyway, when considering the harmonic suppression effect, it is necessary to avoid high k_e or f_{BW}, so as to ensure the estimation accuracy.

Fig. 14(a)–(c) is merged together into Fig. 14(d) where L_g is set as 15 mH. According to the analysis in Section IV, too small k_e will lead to the decrease of SOGI-PLL bandwidth, and then affects the transient response. When the SRF-PLL bandwidth f_{BW} is very small, the SOGI-PLL nonlinearity will be weakened, but the PLL bandwidth will also be greatly reduced, resulting in poor dynamic performance again. In addition, if k_e is too large, the filtering effect of SOGI will be deteriorated and the estimation accuracy will be affected. As can be seen from Fig. 14(d), after considering all the four factors, the optional parameter region is an approximately-triangular region. This fact indicates that parameters of SOGI-PLL might be difficult to be optimized under very weak grid.

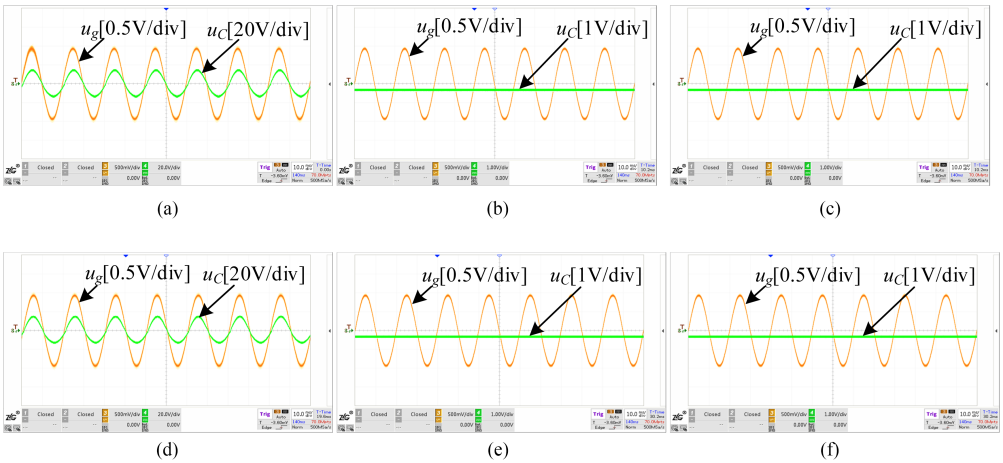

Fig. 20. Experimental waveforms of SOGI-PLL under different f_{BW} and k_e. (a) $k_e = 1.414, f_{\mathrm{BW}} = 100$ Hz. (b) $k_e = 1.414, f_{\mathrm{BW}} = 150$ Hz. (c) $k_e = 1.414, f_{\mathrm{BW}} = 200$ Hz. (d) $k_e = 4, f_{\mathrm{BW}} = 100$ Hz. (e) $k_e = 4, f_{\mathrm{BW}} = 150$ Hz. (f) $k_e = 4, f_{\mathrm{BW}} = 200$ Hz.

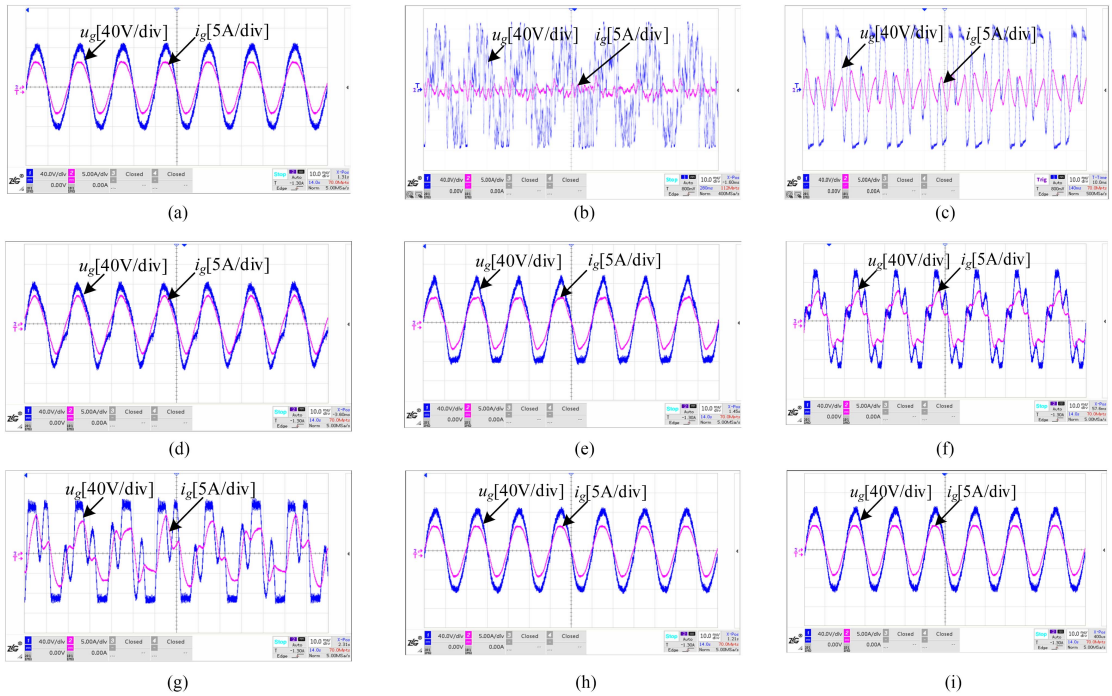

Fig. 21. Experimental waveforms of GCI with SOGI-PLL under different f_{BW}, k_e and L_g. (a) $k_e = 1.414, f_{\mathrm{BW}} = 100$ Hz, $L_g = 10$ mH. (b) $k_e = 1.414, f_{\mathrm{BW}} = 150$ Hz, $L_g = 10$ mH. (c) $k_e = 1.414, f_{\mathrm{BW}} = 100$ Hz, $L_g = 15$ mH. (d) $k_e = 4, f_{\mathrm{BW}} = 100$ Hz, $L_g = 10$ mH. (e) $k_e = 4, f_{\mathrm{BW}} = 100$ Hz, $L_g = 15$ mH. (f) $k_e = 1.414, f_{\mathrm{BW}} = 120$ Hz, $L_g = 10$ mH. (g) $k_e = 1.414, f_{\mathrm{BW}} = 120$ Hz, $L_g = 15$ mH. (h) $k_e = 1.8, f_{\mathrm{BW}} = 80$ Hz, $L_g = 10$ mH. (i) $k_e = 1.8, f_{\mathrm{BW}} = 80$ Hz, $L_g = 15$ mH.

Finally, a step-by-step design procedure for the SOGI-PLL is elaborated in Fig. 15, where $h_{att}()$ denotes the aforementioned attenuations at f_1, f_2, and so on. Refer to the main text for detail.

VI. Extension to the LPF-SOGI-PLL

In the digital control implementation, a low-pass filter (LPF) is usually added to the frequency feedback branch, becoming the LPF-SOGI-PLL, in order to filter out harmonics and noise introduced by the input signal and the digital implementation. In this section, based on the model derived in Section III, the mathematical model of the LPF-SOGI-PLL is derived and the relevant parameters are optimized.

A. Modeling of the LPF-SOGI-PLL

The transfer function of the LPF used in [28] is

$$G_{\mathrm{LPF}}(s) = \frac{2\pi f_{\mathrm{LPF}}}{s + 2\pi f_{\mathrm{LPF}}} \tag{39}$$

where f_{LPF} is the cutoff frequency of the LPF.

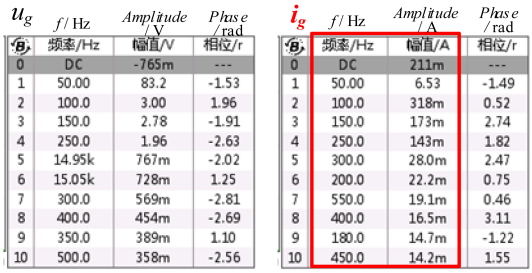

u_g	f / Hz	Amplitude / V	Phase / rad	i_g	f / Hz	Amplitude / A	Phase / rad
	频率/Hz	幅值/V	相位/r		频率/Hz	幅值/A	相位/r
0	DC	-765m	---	0	DC	211m	---
1	50.00	83.2	-1.53	1	50.00	6.53	-1.49
2	100.0	3.00	1.96	2	100.0	318m	0.52
3	150.0	2.78	-1.91	3	150.0	173m	2.74
4	250.0	1.96	-2.63	4	250.0	143m	1.82
5	14.95k	767m	-2.02	5	300.0	28.0m	2.47
6	15.05k	728m	1.25	6	200.0	22.2m	0.75
7	300.0	569m	-2.81	7	550.0	19.1m	0.46
8	400.0	454m	-2.69	8	400.0	16.5m	3.11
9	350.0	389m	1.10	9	180.0	14.7m	-1.22
10	500.0	358m	-2.56	10	450.0	14.2m	1.55

(a)

u_g	f / Hz	Amplitude / V	Phase / rad	i_g	f / Hz	Amplitude / A	Phase / rad
	频率/Hz	幅值/V	相位/r		频率/Hz	幅值/A	相位/r
0	DC	-683m	---	0	DC	293m	---
1	50.00	73.1	-1.49	1	50.00	6.74	-1.43
2	150.0	11.5	-3.08	2	150.0	512m	1.74
3	100.0	6.27	1.79	3	100.0	432m	0.34
4	250.0	1.44	2.84	4	250.0	70.5m	0.47
5	200.0	909m	-1.54	5	350.0	45.4m	2.54
6	14.95k	769m	-1.79	6	130.0	31.0m	1.52
7	15.05k	742m	1.35	7	200.0	25.2m	3.13
8	130.0	620m	2.91	8	70.00	24.9m	2.23
9	350.0	599m	-2.16	9	400.0	23.2m	-2.41
10	400.0	551m	-1.99	10	300.0	18.6m	-2.91

(b)

Fig. 22. Detailed FFT results of u_g, i_g under different condition. (a) $k_e = 1.414, f_{\rm BW} = 100$ Hz, $L_g = 10$ mH. (b) $k_e = 4, f_{\rm BW} = 100$ Hz, $L_g = 10$ mH.

Looking back the entire modeling process for the SOGI-PLL, it is found that the addition of the LPF only affects step 1. Hence, (22)–(25) should be modified for the LPF-SOGI-PLL as

$$u_\alpha(s+j\omega_1) = P_{\alpha-\rm LPF}(s)\Omega_{\rm PLL}(s) + G_\alpha(s+j\omega_1)u_g(s+j\omega_1) \tag{40}$$

$$u_\beta(s+j\omega_1) = P_{\beta-\rm LPF}(s)\Omega_{\rm PLL}(s) + G_\beta(s+j\omega_1)u_g(s+j\omega_1) \tag{41}$$

$$u_\alpha(s-j\omega_1) = N_{\alpha-\rm LPF}(s)\Omega_{\rm PLL}(s) + G_\alpha(s-j\omega_1)u_g(s-j\omega_1) \tag{42}$$

$$u_\beta(s-j\omega_1) = N_{\beta-\rm LPF}(s)\Omega_{\rm PLL}(s) + G_\beta(s-j\omega_1)u_g(s-j\omega_1) \tag{43}$$

where $P_{\alpha\text{-LPF}}(s)$ is the product of $P_\alpha(s)$ and $G_{\rm LPF}(s)$, and $P_{\beta\text{-LPF}}(s)$, $N_{\alpha\text{-LPF}}(s)$, and $N_{\beta\text{-LPF}}(s)$ follow the same notations.

Finally, the transfer function of LPF-SOGI-PLL is obtained

$$G_{\rm LPF-SOGI-PLL}(s) = -\frac{G_{p-\rm LPF}(s-j\omega_1) - G_{n-\rm LPF}(s+j\omega_1)}{2j} \tag{44}$$

where the transfer functions of $G_{p\text{-LPF}}(s)$ and $G_{n\text{-LPF}}(s)$ are expressed in (45) and (46), as shown at the bottom of this page.

To verify the accuracy of the mathematical model of LPF-SOGI-PLL, a similar point-by-point simulation test is done and the corresponding measurement results are shown in Fig. 16. During the test, the parameters of the LPF-SOGI-PLL are: $k_e = 1.414$, $k_{p\_pll} = 0.69$, and $k_{i\_pll} = 75$. In Fig. 12, in accordance with reference [28], $f_{\rm LPF}$ is set as 10 Hz. Again, the proposed way of modeling is verified.

B. Discussions on Parameter Design of the LPF-SOGI-PLL

There are three variables in the LPF-SOGI-PLL, i.e., $k_e, f_{\rm BW}$ and LPF cutoff frequency $f_{\rm LPF}$. According to Section III, a suitable balance for the SOGI-PLL is made when k_e falls in the range [1.6, 2], which is also used for the LPF-SOGI-PLL. With $k_e = 1.7$, Fig. 17 shows the optional parameter range of the LPF-SOGI-PLL when the PLL stability, GCI stability, harmonics suppression, and PLL dynamic performance are all considered.

As can be seen from Fig. 17, if $f_{\rm LPF}$ is lower than 40 Hz, the optional range of $f_{\rm BW}$ is relatively large. When $f_{\rm LPF}$ is increased to 50 Hz, the optional upper limit of $f_{\rm BW}$ has been reduced to about 100 Hz. This indicates that, for the LPF-SOGI-PLL, the cutoff frequency $f_{\rm LPF}$ must be relatively low. From another point of view, when $f_{\rm LPF}$ is small, the influence of the nonlinear frequency feedback loop coupling is greatly weakened so that the frequency estimated by the PLL (i.e., $\omega_{\rm PLL}$) is approximately a constant, and the frequency characteristics of the LPF-SOGI-PLL will be much closer to the FFSOGI-PLL.

VII. Experimental Validations

To verify the above analysis, a single-phase T-type neutral-point-clamped (TNPC) grid-connected inverter has been built in the lab, and the sampling and control are realized by DSP TMS320F28335. Specially, the two integrators in the SOGI are discretized with the third-order discretization technique in order to avoid the algebraic loop problem and to obtain the highest accuracy [9], [33]. To avoid the possible harmonics oscillation in the experimental process, the following experiments are carried out at a lower voltage level for safety reasons. In the test, the parameters of *LCL* filter are still the same as those in Table I, but the grid voltage and the grid current are reduced to a quarter of those in Table I. Thus, SCR = 3 still corresponds to $L_g = 10$ mH and SCR = 2 corresponds to $L_g = 15$ mH.

Note that the behavior of the PLL is hard to be measured during the grid-connected operation of overall inverter system. Hence, to test the phase locking and stability of the PLL itself, the following way is used. The inverter prototype is operated under standalone mode. The signal generator DG4062 is used to generate a sinusoidal signal with peak-to-peak value of 2 V and frequency of 50 Hz to simulate the grid voltage. Since the prototype does not employ digital-to-analog conversion module, in order to capture the PLL output, an open-loop modulation wave (denoted as u_m) is constructed by using the PLL output

$$G_{p-\rm LPF}(s) = \frac{T_{\rm PLL}(s)\cdot[-jG_\alpha(s+j\omega_1) + G_\beta(s+j\omega_1)]}{2 - sT_{\rm PLL}(s)\boldsymbol{G}_{\rm LPF}(\boldsymbol{s})\cdot[-jP_\alpha(s) + jN_\alpha(s) + P_\beta(s) + N_\beta(s)]} \tag{45}$$

$$G_{n-\rm LPF}(s) = \frac{T_{\rm PLL}(s)\cdot[jG_\alpha(s-j\omega_1) + G_\beta(s-j\omega_1)]}{2 - sT_{\rm PLL}(s)\boldsymbol{G}_{\rm LPF}(\boldsymbol{s})\cdot[-jP_\alpha(s) + jN_\alpha(s) + P_\beta(s) + N_\beta(s)]}. \tag{46}$$

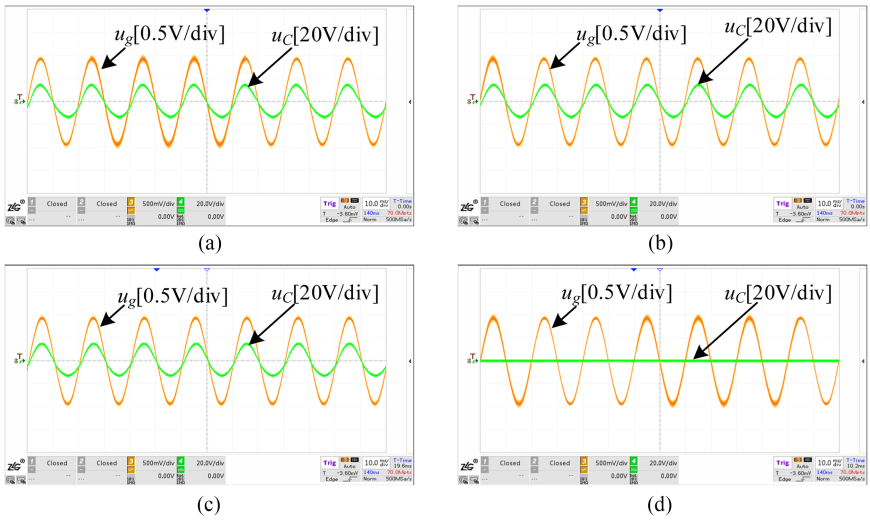

Fig. 23. Experimental waveforms of LPF-SOGI-PLL under different $f_{\rm BW}$ and $f_{\rm LPF}$. (a) $f_{\rm BW} = 100$ Hz, $f_{LPF} = 10$ Hz. (b) $f_{\rm BW} = 150$ Hz, $f_{\rm LPF} = 10$ Hz. (c) $f_{\rm BW} = 100$ Hz, $f_{\rm LPF} = 50$ Hz. (d) $f_{\rm BW} = 150$ Hz, $f_{\rm LPF} = 50$ Hz.

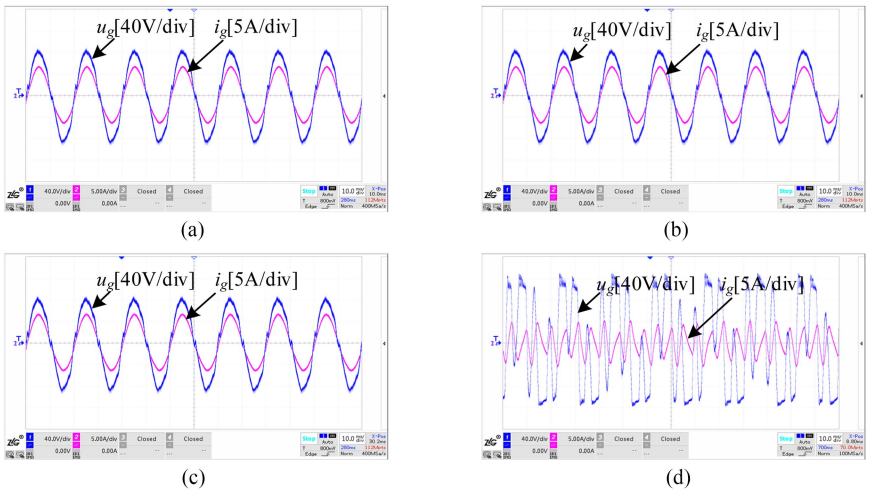

Fig. 24. Experimental waveforms of GCI with LPF-SOGI-PLL under different $f_{\rm BW}$ and $f_{\rm LPF}$ for $L_g = 15$ mH. (a) $f_{\rm BW} = 100$ Hz, $f_{\rm LPF} = 10$ Hz. (b) $f_{\rm BW} = 150$ Hz, $f_{\rm LPF} = 10$ Hz. (c) $f_{\rm BW} = 100$ Hz, $f_{\rm LPF} = 50$ Hz. (d) $f_{\rm BW} = 150$ Hz, $f_{\rm LPF} = 50$ Hz.

phase and the sine table in the DSP, and then is sent to the PWM module. Consequently, the inverter output u_{inv} (see Fig. 1) under the standalone mode can be the same in phase with u_m. Then, to approximately observe the PLL estimated phase, we only need to observe u_C, which is filtered by an *LC* filter in Fig. 1.

For the rest tests, the GCI is operated under grid-connected mode, connecting to the ac grid.

A. Start-Up and Transient Performances

Fig. 18 shows the start-up waveforms of the GCI. Once all the power units are powered up and the power-on button is pressed, the grid-side relay is closed and then the DSP wll run the A/D conversion interrupt service routine, in which the PLL algorithm will be activated. And, after the PLL obtains the phase of the grid voltage, the amplitude of the grid current reference is increased gradually until it reaches the desired value (here, 8 A).

To present the transient operation of the SOGI-PLL with frequency change, an independent DSP development board is adopted to run the PLL routine. The input voltage $u_g = 1.65 + 0.25 \sin(2\pi f_1 t)$ is generated by DG4062 and then sent to the DSP. The desired variables (e.g., $f_{\rm PLL}$ and i_{ref}) are output with the help of the 8-bit chip TLV5620 whose output ranges 0–255.

Fig. 19 illustrates the frequency responses of the SOGI-PLL under a frequency jump from 50–55 Hz. To clearly present the exact point of frequency jump (denoted as t_1), the amplitude of u_g is simultaneously decreased by 20% at t_1. Seen from Fig. 19(a), i_{ref} synchronizes with u_g quickly under a frequency jump. In Fig. 19(b), the estimated frequency $f_{\rm PLL}$ is filtered by a digital LPF of 12 Hz in the oscilloscope to distinctly reveal the tracking performance. Obviously, $f_{\rm PLL}$ can track the input frequency

quickly and accurately. In Fig. 19(c), the FFT result of the unfiltered f_{PLL} shows that the even components shown in Fig. 4 do exist. Note that the 50 Hz-component in f_{PLL} is generated by the dc component in u_g (originally caused by DG4062) and is not cancelled completely in the independent DSP board due to fixed-point calculation. Excluding the 50 Hz-component, the dominant harmonic content in f_{PLL} is located at 100 Hz, which agrees with the simulation results in Fig. 4 and the assumption about ω_{PLL} in Section III.

B. Validation of the Stability With SOGI-PLL

Fig. 20 shows the experimental waveforms of the SOGI-PLL operation under different f_{BW} and k_e. In the figure, u_g [1 V/div] corresponds to the actual PCC voltage u_g [55 V/div]. Seen from Fig. 20, with the same SOGI parameter k_e, when the bandwidth of SRF-PLL changes from 100–200 Hz, the SOGI-PLL output (reflected by u_C) is abnormal and the instability of SOGI-PLL itself is observed. Moreover, during the test, under the high f_{BW} (e.g., 200 Hz), the PLL output frequency and phase can be very sensitive to noises, challenging the feedback of f_{PLL} into SOGI. Then, for SOGI-PLL without filters on the frequency feedback path, noises can make the PLL ineffective even if k_e is increased up to 4. Nevertheless, high f_{BW} is not recommended.

Furthermore, Fig. 21 shows some experimental waveforms of the GCI under different k_e, f_{BW}, and L_g. Corresponding points taken for test in Fig. 21 are labeled in Fig. 14(d). With $k_e = 1.414$, $f_{\mathrm{BW}} = 100$ Hz, and $L_g = 10$ mH, although there are some harmonics in u_g, few harmonics can be seen in i_g. In this case, the SOGI-PLL is normally phase locked and the inverter runs stably. However, if f_{BW} is increased to 150 Hz, the GCI becomes unstable. If L_g is increased to 15 mH, the GCI is also unstable and both i_g and u_g are highly distorted. Under the conditions shown in Fig. 21(c), increasing k_e to 4 can make the inverter stable again. However, the harmonics in i_g in Fig. 21(d) is significantly higher than that shown in Fig. 21(a), which is caused by the increase of k_e. To be clearer, the detailed harmonic contents in both u_g and i_g are provided in Fig. 22. Note that the third-order harmonics is significantly increased with k_e increasing from 1.414–4 and so as to the 100 Hz harmonic, which results in a more distorted i_g in consequence. Specially, the 150 Hz-component becomes larger than the 100 Hz-component when k_e increases from 1.414–4. This is mainly caused by the worse harmonic attenuation of the SOGI at harmonics frequencies. When the selected parameters locate in the recommended region in Fig. 14(d) [waveforms are given in Fig. 21(h) and (i)], the GCI works well even under $L_g = 15$ mH, which validates the analysis and design in Section V.

Based on the theoretical analysis in Section IV-D and the stability records in Fig. 20(c) and (b), Table V shows the comparisons of different models in Cases I and II. The accuracy of the proposed model is verified.

C. Validation of the Stability With LPF-SOGI-PLL

Fig. 23 shows the experimental waveforms of the LPF-SOGI-PLL operation under different f_{BW} and f_{LPF}. According to Fig. 23(a) and (b), when f_{LPF} is 10 Hz, whatever f_{BW} is 100 or 150 Hz, the PLL can work stably. When f_{LPF} increases to 50 Hz, the PLL is still stable when the f_{BW} is 100 Hz, but unstable when f_{BW} increases to 150 Hz. This indicates that f_{LPF} must be very low to enable the stable operation of the PLL so that the nonlinear coupling effect in the SOGI-PLL is well suppressed. The abovementioned experimental results verify the analysis of the LPF-SOGI-PLL model proposed in Section IV.

Fig. 24 shows the experimental waveforms of the GCI under different f_{BW} and f_{LPF} for $L_g = 15$ mH. As can be seen from Fig. 24, when f_{LPF} is 10 Hz, the GCI is stable regardless of the value of f_{BW}. If f_{LPF} increases from 10–50 Hz, the GCI is still stable when f_{BW} is still 100 Hz. But if f_{BW} continues to increase to 150 Hz, the GCI loses stability. This once again shows that f_{LPF} must be very low to ensure the stability of the GCI.

VIII. Conclusion

Aiming at the nonlinear coupling caused by the FFL in the SOGI-PLL, an accurate SOGI-PLL model taking into account the influence of FFL has been proposed. Based on the newly-established model, impacts of PLL parameters on the behavior of the PLL itself and the stability of the inverter are analyzed, and a graphical parameter design method of the SOGI-PLL and LPF-SOGI-PLL are proposed. Conclusions include the following.

1) With the FFL effect considered, the proposed model for the SOGI-PLL is more accurate than those ignoring the FFL. Specially, the resonant peak caused by the FFL is found and is proved to have serious effect on the stability.
2) Based on the proposed model, the parameters (i.e., k_e, f_{BW}) effect is analyzed and the instability mechanism is revealed. Specially, the increase of k_e can help suppress the resonant peak caused by FFL. But, the increase of f_{BW} enlarges the dc gain of the SOGI-PLL and causes the sharp increase of the resonant peak so that the stability of the PLL itself and that of the GCI are more seriously endangered. Note that these results differ much from those revealed by previous models without considering the FFL effect.
3) In view of abovementioned effects, parameters of the SOGI-PLL are difficult to design if several factors mentioned in Section V are considered simultaneously. Hence, a graphical method of parameters selection is proposed to improve the overall performance under nonideal grid conditions.
4) Incorporating the LPF on the frequency feedback path from SRF-PLL to SOGI can help reduce the nonlinear coupling effect of FFL. And selecting a low cutoff frequency for the LPF-SOGI-PLL is simple yet beneficial to the performance of the GCI under the weak grid.

References

[1] D. P. Morán-Río, J. Roldán-Pérez, M. Prodanović, and A. García-Cerrada, "Influence of the phase-locked loop on the design of microgrids formed by diesel generators and grid-forming converters," *IEEE Trans. Power Electron.*, vol. 37, no. 5, pp. 5122–5137, May 2022.

[2] H. Gong, X. Wang, and L. Harnefors, "Rethinking current controller design for PLL-Synchronized VSCs in weak grids," *IEEE Trans. Power Electron.*, vol. 37, no. 2, pp. 1369–1381, Feb. 2022.
[3] J. Xu, S. Bian, Q. Qian, H. Qian, and S. Xie, "Robustness improvement of single-phase inverters under weak grid cases by adding grid current feedforward in delay-based phase-locked loop," *IEEE Access*, vol. 8, pp. 124275–124287, 2020.
[4] Y. Han, M. Luo, X. Zhao, J. M. Guerrero, and L. Xu, "Comparative performance evaluation of orthogonal-signal-generators-based single-phase PLL Algorithms—A survey," *IEEE Trans. Power Electron.*, vol. 31, no. 5, pp. 3932–3944, May 2016.
[5] Y. Yang, K. Zhou, and F. Blaabjerg, "Virtual unit delay for digital frequency adaptive T/4 delay phase-locked loop system," in *Proc. IEEE 8th Int. Power Electron. Motion Control Conf.*, 2016, pp. 2910–2916.
[6] I. Galkin and M. Vorobyov, "Optimizing of sampling in a low-cost single-phase instantaneous AC-grid synchronization unit with discrete calculation of derivative function," in *Proc. 41st Annu. Conf. IEEE Ind. Electron. Soc.*, 2015, pp. 004538–004543.
[7] R. M. Santos Filho, P. F. Seixas, P. C. Cortizo, L. A. B. Torres, and A. F. Souza, "Comparison of three single-phase PLL algorithms for UPS applications," *IEEE Trans. Ind. Electron.*, vol. 55, no. 8, pp. 2923–2932, Aug. 2008.
[8] P. Hao, W. Zanji, and C. Jianye, "A measuring method of the single-phase AC frequency, phase, and reactive power based on the Hilbert filtering," *IEEE Trans. Instrum. Meas.*, vol. 56, no. 3, pp. 918–923, Jun. 2007.
[9] M. Ciobotaru, R. Teodorescu, and F. Blaabjerg, "A new single-phase PLL structure based on second order generalized integrator," in *Proc. 37th IEEE Power Electron. Specialists Conf.*, 2006, pp. 1–6.
[10] J. Xu, H. Qian, S. Bian, Y. Hu, and S. Xie, "Comparative study of single-phase phase-locked loops for grid-connected inverters under non-ideal grid conditions," *CSEE J. Power Energy Syst.*, vol. 8, no. 1, pp. 155–164, Jan. 2022.
[11] S. Golestan, S. Y. Mousazadeh, J. M. Guerrero, and J. C. Vasquez, "A critical examination of frequency-fixed second-order generalized integrator-based phase-locked loops," *IEEE Trans. Power Electron.*, vol. 32, no. 9, pp. 6666–6672, Sep. 2017.
[12] M. S. Reza, M. Ciobotaru, and V. G. Agelidis, "Tracking of time-varying grid voltage using DFT based second order generalized integrator technique," in *Proc. IEEE Int. Conf. Power Syst. Technol.*, 2012, pp. 1–6.
[13] G. Fedele, C. Picardi, and D. Sgro, "A power electrical signal tracking strategy based on the modulating functions method," *IEEE Trans. Ind. Electron.*, vol. 56, no. 10, pp. 4079–4087, Oct. 2009.
[14] A. Sahoo, K. Mahmud, M. Ciobotaru, and J. Ravishankar, "Adaptive grid synchronization technique for Single-phase inverters in AC microgrid," in *Proc. IEEE Energy Convers. Congr. Expo.*, 2019, pp. 4441–4446.
[15] M. S. Reza, M. Ciobotaru, and V. G. Agelidis, "Estimation of single-phase grid voltage fundamental parameters using fixed frequency tuned second-order generalized integrator based technique," in *Proc. 4th IEEE Int. Symp. Power Electron. Distrib. Gener. Syst.*, 2013, pp. 1–8.
[16] F. Xiao, L. Dong, L. Li, and X. Liao, "A frequency-fixed SOGI-Based PLL for single-phase grid-connected converters," *IEEE Trans. Power Electron.*, vol. 32, no. 3, pp. 1713–1719, Mar. 2017.
[17] Q. Guan, Y. Zhang, Y. Kang, and J. M. Guerrero, "Single-Phase phase-locked loop based on derivative elements," *IEEE Trans. Power Electron.*, vol. 32, no. 6, pp. 4411–4420, Jun. 2017.
[18] F. D. Freijedo, J. Doval-Gandoy, O. Lopez, and E. Acha, "Tuning of phase-locked loops for power converters under distorted utility conditions," *IEEE Trans. Ind. Appl.*, vol. 45, no. 6, pp. 2039–2047, Nov./Dec. 2009.
[19] S. Golestan, M. Monfared, F. D. Freijedo, and J. M. Guerrero, "Dynamics assessment of advanced single-phase PLL structures," *IEEE Trans. Ind. Electron.*, vol. 60, no. 6, pp. 2167–2177, Jun. 2013.
[20] C. Zhang, X. Wang, F. Blaabjerg, W. Wang, and C. Liu, "The influence of phase-locked loop on the stability of single-phase grid-connected inverter," in *Proc. IEEE Energy Convers. Congr. Expo.*, 2015, pp. 4737–4744.
[21] H. Zhang, Z. Liu, S. Wu, and Z. Li, "Input impedance modeling and verification of single-phase voltage source converters based on harmonic linearization," *IEEE Trans. Power Electron.*, vol. 34, no. 9, pp. 8544–8554, Sep. 2019.
[22] C. Zhang, M. Molinas, S. Føyen, J. A. Suul, and T. Isobe, "Harmonic-Domain SISO equivalent impedance modeling and stability analysis of a single-phase grid-connected VSC," *IEEE Trans. Power Electron.*, vol. 35, no. 9, pp. 9770–9783, Sep. 2020.
[23] C. Zhang, S. Føyen, J. A. Suul, and M. Molinas, "Modeling and analysis of SOGI-PLL/FLL-Based synchronization units: Stability impacts of different frequency-feedback paths," *IEEE Trans. Energy Convers.*, vol. 36, no. 3, pp. 2047–2058, Sep. 2021.
[24] J. Lei, X. Quan, S. Feng, J. Zhao, and W. Chen, "Accurate modeling of PLL with frequency-adaptive prefilter: On the positive feedback effect," *IEEE Trans. Power Electron.*, vol. 37, no. 4, pp. 3747–3752, Apr. 2022.
[25] D. Yang, X. Ruan, and H. Wu, "A real-time computation method with dual sampling mode to improve the current control performance of the LCL-Type grid-connected inverter," *IEEE Trans. Ind. Electron.*, vol. 62, no. 7, pp. 4563–4572, Jul. 2015.
[26] J. Sun, "Impedance-Based stability criterion for grid-connected inverters," *IEEE Trans. Power Electron.*, vol. 26, no. 11, pp. 3075–3078, Nov. 2011.
[27] S. Shah and L. Parsa, "Impedance modeling of three-phase voltage source converters in DQ, sequence, and phasor domains," *IEEE Trans. Energy Convers.*, vol. 32, no. 3, pp. 1139–1150, Sep. 2017.
[28] S. Shah, P. Koralewicz, V. Gevorgian, and L. Parsa, "Small-Signal modeling and design of phase-locked loops using harmonic signal-flow graphs," *IEEE Trans. Energy Convers.*, vol. 35, no. 2, pp. 600–610, Jun. 2020.
[29] Y. Wang, X. Chen, Y. Zhang, J. Chen, and C. Gong, "Impedance modeling of three-phase grid-connected inverters and analysis of interaction stability in grid-connected system," in *Proc. IEEE 8th Int. Power Electron. Motion Control Conf.*, 2016, pp. 3606–3612.
[30] J. Xu, Q. Qian, B. Zhang, and S. Xie, "Harmonics and stability analysis of single-phase grid-connected inverters in distributed power generation systems considering phase-locked loop impact," *IEEE Trans. Sustain. Energy*, vol. 10, no. 3, pp. 1470–1480, Jul. 2019.
[31] D. Zhu, S. Zhou, X. Zou, Y. Kang, and K. Zou, "Small-Signal disturbance compensation control for LCL-Type grid-connected converter in weak grid," *IEEE Trans. Ind. Appl.*, vol. 56, no. 3, pp. 2852–2861, May/Jun. 2020.
[32] X. Chen, Y. Zhang, S. Wang, J. Chen, and C. Gong, "Impedance-Phased dynamic control method for grid-connected inverters in a weak grid," *IEEE Trans. Power Electron.*, vol. 32, no. 1, pp. 274–283, Jan. 2017.
[33] M. -S. Karbasforooshan and M. Monfared, "An improved reference current generation and digital deadbeat controller for single-phase shunt active power filters," *IEEE Trans. Power Del.*, vol. 35, no. 6, pp. 2663–2671, Dec. 2020.

Jinming Xu (Member, IEEE) was born in Xuzhou, China, in 1987. He received the B.S. degree in electrical engineering and the Ph.D. degree in power electronics from Nanjing University of Aeronautics and Astronautics (NUAA), Nanjing, China, in 2009 and 2017, respectively.

In 2017, he was with the College of Automation Engineering, NUAA, where he has been an Associate Professor since 2020. He has authored and coauthored more than 100 technical papers in international journals and conference proceedings. His current research interests include the grid-connected inverters and control, and renewable power generations.

Dr. Xu was a recipient of the 2015 IET Power Electronics Premium Award. He received the Excellent Doctoral Dissertations Award from Jiangsu Province, China, in 2018, and the Third Prize of 2021 Jiangsu Provincial Science and Technology Award. He was recognized as one of IEEE TRANSACTIONS ON POWER ELECTRONICS' Outstanding Reviewers of 2020.

Hao Qian was born in Huaian, China, in 1997. He received the B.S. and M.S. degrees in electrical engineering from Nanjing University of Aeronautics and Astronautics (NUAA), Nanjing, China, in 2019 and 2022, respectively.

His current research interests mainly include the grid-connected inverter and control strategies.

Qiang Qian (Member, IEEE) was born in Xuancheng, China, in 1992. He received the B.S. degree in electrical engineering and the Ph.D. degree in power electronics from the Nanjing University of Aeronautics and Astronautics (NUAA), Nanjing, China, in 2012 and 2019, respectively.

In 2019, he was with the College of Energy and Electrical Engineering, Hohai University, where he is currently a lecture. His research interests include the modeling and the control of the multiparallel grid-connected inverters.

Shaojun Xie (Member, IEEE) was born in Hubei Province, China, in 1968. He received the B.S., M.S., and Ph.D. degrees in electrical engineering from the Nanjing University of Aeronautics and Astronautics (NUAA), Nanjing, China, in 1989, 1992, and 1995, respectively.

In 1992, he was with the Faculty of Electrical Engineering Teaching and Research Division, NUAA, where he is currently a Professor with the College of Automation Engineering. In recent five years, he has authored and coauthored more than 100 technical papers published in many international journals and conference proceedings. His main research interests include the aviation electrical power supply and power electronic conversion.

Prof. Xie was a recipient of the 2015 IET Power Electronics Premium Award.